

# Working Mechanism for Flexible Perovskite Solar Cells with Simplified Architecture

Xiaobao Xu,<sup>†,‡</sup> Qi Chen,<sup>†</sup> Ziruo Hong,<sup>†</sup> Huanping Zhou,<sup>†</sup> Zonghao Liu,<sup>†,‡</sup> Wei-Hsuan Chang,<sup>†</sup> Pengyu Sun,<sup>†</sup> Huajun Chen,<sup>†</sup> Nicholas De Marco,<sup>†</sup> Mingkui Wang,<sup>\*,‡</sup> and Yang Yang<sup>\*,†</sup>

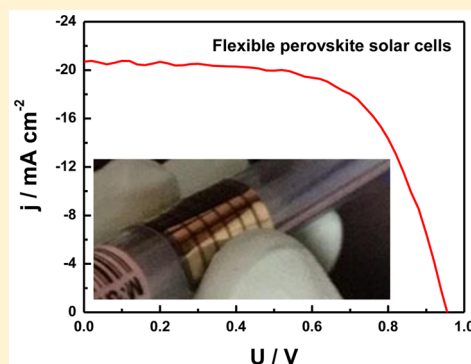
<sup>†</sup>Department of Materials Science and Engineering, University of California, Los Angeles, California 90095, United States

<sup>‡</sup>Wuhan National Laboratory for Optoelectronics, School of Optical, Electronic Information, Huazhong University of Science, Technology, Wuhan, Hubei 430074, People's Republic of China

## S Supporting Information

**ABSTRACT:** In this communication, we report an efficient and flexible perovskite solar cell based on formamidinium lead trihalide (FAPbI<sub>3</sub>) with simplified configuration. The device achieved a champion efficiency of 12.70%, utilizing direct contact between metallic indium tin oxide (ITO) electrode and perovskite absorber. The underlying working mechanism is proposed subsequently, via a systematic investigation focusing on the heterojunction within this device. A significant charge storage has been observed in the perovskite, which is believed to generate photovoltage and serves as the driving force for charge transferring from the absorber to ITO electrode as well. More importantly, this simplified device structure on flexible substrates suggests its compatibility for scale-up fabrication, which paves the way for commercialization of perovskite photovoltaic technology.

**KEYWORDS:** Perovskite, solar cell, heterojunction, built-in potential, working mechanism



Inorganic/organic hybrid metal halide perovskites, enabling the assembly of organic and inorganic components within a single molecular-scale, represents a family of unique semiconductors featured with compositional versatility and superior optoelectronic properties such as excellent defects tolerance, suitable band structure, ambipolar carrier transport, and long carrier lifetime.<sup>1–4</sup> They have been found to have promising applications in high-performance optoelectronics, especially as photovoltaic cells.<sup>5–7</sup> The power conversion efficiency (PCE) has rapidly increased to over 20% in perovskite solar cells<sup>8</sup> following the initial report in 2009.<sup>9</sup> Now that perovskite technology has been regarded as a serious player in the photovoltaic field, it has the potential to compete with crystalline silicon solar cells.

In planar type perovskite solar cells, the devices adopt layer-to-layer configuration, where the perovskite absorber layer is sandwiched by both electron/hole transport layers (ETL/HTL).<sup>10,11</sup> Upon irradiation, carriers are generated in the perovskite layer, extracted by the adjacent ETL and HTL and eventually collected by electrodes. Metal oxide materials such as TiO<sub>2</sub> are widely used as ETL in perovskite solar cells for their mature application in the photovoltaic field.<sup>2,12,13</sup> The TiO<sub>2</sub> layer, however, requires a high-temperature sintering process to obtain intimate contact, whereas for manufacturing purposes it is desirable to obtain low temperature processes.<sup>14</sup> Even a compact layer of TiO<sub>2</sub> with a thickness of tens of nanometers in planar perovskite solar cells needs sub-150 °C process,<sup>15,16</sup> which also precludes the use of plastic PET substrates. In order

to translate lab-scale device fabrication to a fab-scale commercial production, it is preferred to obtain a proper selective layer that requires a low-temperature process, for example, the solar cell can be constructed on flexible polymer-based substrates. Until now, a series of laudable attempts to pursue high-performance perovskite solar cells with low-temperature process based on organic charge transport materials<sup>17–19</sup> and inorganic semiconductors like ZnO<sup>20,21</sup> have been reported. As one step forward, a more simplified device architecture is believed to be more important for reducing the issues due to mass process in device fabrication. Recently, it has also been documented that decent PCEs are able to be achieved in devices without either HTL<sup>22,23</sup> or ETL.<sup>24,25</sup> Despite the practical demonstrations, the details regarding the working mechanisms in such a device remain unclear,<sup>26,27</sup> for example, how carriers behave within the perovskite thin film and further build up the photovoltage in such devices. Thus, it becomes desirable to gain further insight into the transport layer-free devices.

In this work, we systematically explored a simplified device without any electron transport layer. First, a formamidinium-based perovskite film deposited directly onto a tin indium oxide (ITO) substrate was used as the photoactive layer due to its narrowed bandgap for spectral match with sun light. A

Received: May 29, 2015

Revised: September 16, 2015

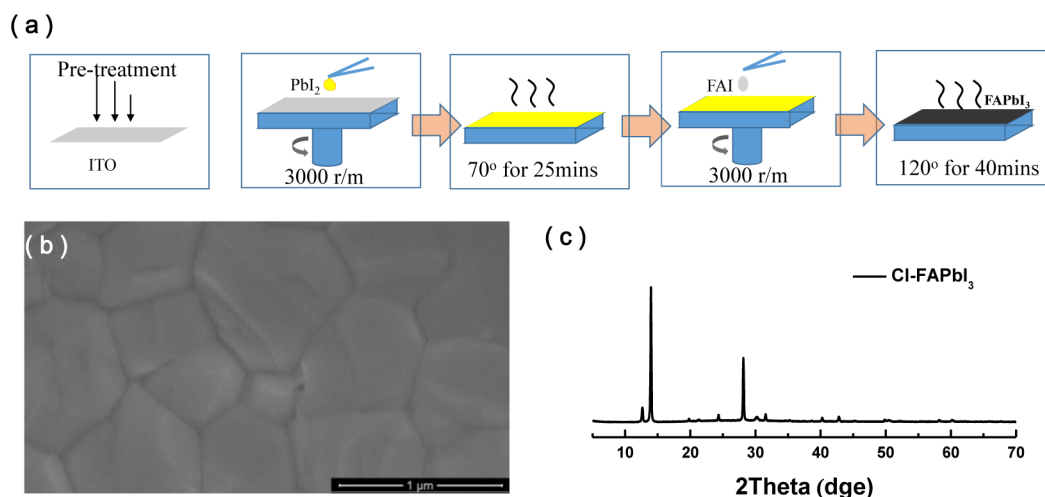


**Figure 1.** Fabrication scheme for perovskite thin film using two-step solution process. (a) Schematic diagram for thin film formation of chlorine-incorporated formamidinium lead trihalide (Cl-FAPbI<sub>3</sub>) perovskite on an ITO substrate, (b) the top-view SEM of the Cl-FAPbI<sub>3</sub> film on ITO<sub>(PET)</sub>, and (c) XRD profile confirming the FAPbI<sub>3</sub> crystals.

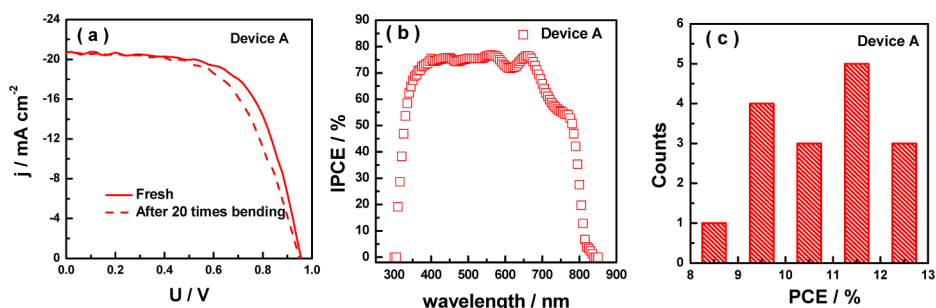


**Figure 2.** Photovoltaic parameters for flexible device A under AM 1.5G illumination (100 mW cm<sup>-2</sup>). (a) Density–potential ( $J$ – $V$ ) characteristics of device A with ITO<sub>(PET)</sub>/Cl-FAPbI<sub>3</sub> (350 nm)/spiro-OMeTAD(150 nm)/Au(100 nm), using a metallic mask with an aperture area of 0.108 cm<sup>2</sup>, while the scan rate was kept at 20 mV per step with a delay time of 0.001 s. The dashed line shows maintained  $J$ – $V$  performance up to 20 times bending for flexible device. (b) Monochromatic incident photon-to-electron conversion efficiency (IPCE) spectrum and (c) histogram of PCE for flexible devices for one batch.

champion PCE of 12.70% was achieved for the flexible perovskite solar cell based on ITO/PET (ITO<sub>(PET)</sub>) substrate, highlighting the great potential of the device design and fabrication process for future roll-to-roll manufacturing. More importantly, photogenerated charge behavior has been carefully probed to illustrate working mechanism of the device by using Kelvin probe force microscopy (KPFM), X-ray diffraction (XRD), ultraviolet photoelectron spectrum (UPS), and capacitance–voltage ( $C$ – $V$ ) analysis. Our results show that a negligible built-in potential was formed across the perovskite/ITO heterojunction, meaning that the built-in potential in this heterojunction is not essential for electron extraction. Moreover, a large capacitance in such device is measured, which could ensure the proper photovoltage and provide concentration carrier concentration gradient that drives charge transfer from perovskite to ITO. Though  $p$ – $i$ – $n$  type device structure still dominates the field, we argue that alternative device design without electron/hole selective contact is promising according to our previous success in HTL free devices.<sup>14,28</sup> Meanwhile, our findings also indicate the potential opportunity for applying various highly conductive materials for perovskite device development.

**Results and Discussion.** The organic cation of the inorganic/organic hybrid perovskite can be used to tune the optical bandgap that provides great versatility in crystal

structure and composition.<sup>29–32</sup> For example, perovskite with a  $\text{CH}(\text{NH}_2)_2^+$  cation, which is larger than  $\text{CH}_3\text{NH}_3^+$ , shows a smaller optical bandgap with promising more efficient infrared light harvesting and corresponding high photocurrent.<sup>33,34</sup> In this work, the hybrid inorganic/organic perovskite was synthesized using  $\text{CH}(\text{NH}_2)_2^+$ , while  $\text{CH}_3\text{NH}_3\text{Cl}$  was used as an additive to provide good film quality with enhanced interfacial opto-electric property via chlorine incorporation.<sup>3,35,36</sup> A two-step solution process was adapted here to synthesize chlorine incorporated  $\text{CH}(\text{NH}_2)_2\text{PbI}_3$  (Cl-FAPbI<sub>3</sub>) as illustrated in Figure 1a (see details in Methods section). The perovskite films were directly formed on ITO substrate without any charge selective layers. Before spin-coating PbI<sub>2</sub> layer, the flexible ITO substrate was treated in UV–ozone for 30 min. Typically UV–ozone treatment increases the work function of ITO film due to the oxidation of the surface and also removes organic residues and enhances surface wetting.<sup>37</sup> Figure 1b provides a top view SEM image of the morphology of the synthesized Cl-FAPbI<sub>3</sub> film on ITO<sub>(PET)</sub> substrate. It shows the clear formation of a uniform, compact Cl-FAPbI<sub>3</sub> layer. We further confirm the Cl-FAPbI<sub>3</sub> crystalline structure using XRD. It is worth emphasizing that the peak at 13° in XRD indicates residual PbI<sub>2</sub> in the as-synthesized Cl-FAPbI<sub>3</sub> compound as discussed later. Contrary to the previous results,<sup>6,34</sup> the sharp diffraction peaks shown in Figure 1c indicate the high

crystallinity of Cl-FAPbI<sub>3</sub> samples<sup>38</sup> with 120 °C annealing procedure, allowing us to further explore its intrinsic physical property and photoelectric properties. An additional XRD profile of Cl-FAPbI<sub>3</sub> stored in air (48% humidity) with the peak of 11.5° indicate a new crystalline phase as shown in [Supporting Information](#) Figure S1, which is assumed to originate from (FA)<sub>4</sub>PbI<sub>6</sub>·2H<sub>2</sub>O due to Cl-FAPbI<sub>3</sub> hydration.<sup>39</sup>

A flexible device with Cl-FAPbI<sub>3</sub> deposited directly on ITO<sub>(PET)</sub> (denoted as device A) is presented. The corresponding photocurrent density–voltage (*J*–*V*) characteristics of devices under AM 1.5G illumination is shown in [Figure 2a](#). The applied voltage scan rate in *J*–*V* measurement was kept at 20 mV per step with a delay time of 0.001 s. A champion PCE of 12.70% for a reverse scan with a short circuit current density (*J*<sub>SC</sub>) of 20.70 mA cm<sup>−2</sup>, an open circuit voltage (*V*<sub>OC</sub>) of 0.955 V, and a fill factor (FF) of 0.64, represent an efficient flexible perovskite photovoltaic cell. It is interesting to note that in the *J*–*V* curve there is some undesired oscillation, which will be discussed later. However, the stabilized power output current density at 0.7 V is presented in [Supporting Information](#) Figure S2 with stable output PCE of 6.8%. Thus, we believe this efficient simplified device without ETL holds huge potential toward the roll-to-roll fabrication. However, devices without CH<sub>3</sub>NH<sub>3</sub>Cl as an additive in the active layer fabrication process had poor performance, as shown in [Supporting Information](#) Figure S3, and this device got rapidly bleached in air. In our previous work, solid evidence has shown that chlorine incorporation can affect not only the formation of perovskite films but also the relevant interface, which results in improved optoelectronic characteristics due to enhanced charge transferring across the heterojunction interface rather than within perovskite crystals.<sup>40</sup> The incident photon-to-current conversion efficiency (IPCE) spectrum for device A is shown in [Figure 2b](#). It shows a response from 305 to 835 nm, which is in good agreement with the optical absorption (presented in [Supporting Information](#) Figure S4). The relatively flat spectral profile approaching 80% is indicative of excellent light harvesting for high photocurrent.<sup>41</sup> For better performance evaluation of this hole-blocking layer-free flexible device A, [Figure 2c](#) gives a histogram showing PCE distribution of those devices in one batch. An average PCE of 11.5% was achieved with half of the devices showing PCE over 11%. The narrow PCE distribution strongly indicates the good reproducibility of our device processing.

In order to determine the robustness in mechanical properties of the flexible devices, a bending test was carried out. After bending 20 times, the *J*–*V* characteristics of device A are shown in [Figure 2a](#) in comparison with the pristine device, and the key photovoltaic parameters are tabulated in [Table 1](#). *V*<sub>OC</sub> and *J*<sub>SC</sub> slightly decreased after bending, and the major PCE loss is also contributed from the degradation in FF. Considering the robustness of each component in this device, the degradation of FF should be ascribed to the increasing

resistance in Au counter electrode because small cracks can be visible by the human eye after bending.

To further understand the working mechanism of this ETL free device two different devices with/without TiO<sub>2</sub> were fabricated on an ITO/glass substrate (ITO<sub>(glass)</sub>). Devices B and C consist of ITO<sub>(glass)</sub>/Cl-FAPbI<sub>3</sub>/spiro-OMeTAD/Au and ITO<sub>(glass)</sub>/TiO<sub>2</sub>/Cl-FAPbI<sub>3</sub>/spiro-OMeTAD/Au, respectively. Cross-sectional SEM images of the two cell configurations are presented in [Supporting Information](#) Figure S5. The *J*–*V* characteristics of the devices under AM1.5G 1 sun illumination are given in [Figure 3a](#). The detailed photovoltaic parameters, that is, *V*<sub>OC</sub>, FF, *J*<sub>SC</sub>, and PCE for devices B and C are tabulated in [Table 2](#). A PCE of 15.45% was achieved in device B without ETL, comparable to that of 15.32% in reference cell, device C, with TiO<sub>2</sub> as ETL. Unfortunately, the undesired oscillation also appears in *J*–*V* curves for device B. For each point in the *I*–*V* curve, the product of the current and voltage represents the output power for that operating condition. The measurement of photocurrent in each applied voltage is observed to take a certain period of time to reach the constant state in the test cell, which depends on intrinsic properties of the device. Generally, the delay time is 4 times as long as the time constant, which is time for reaching (1 − 1/*e*) of photocurrent response to the applied bias.<sup>42</sup> As shown in [Supporting Information](#) Figure S6, it is *J*–*V* curves as illustration for devices containing ITO<sub>(PET)</sub>/Cl-FAPbI<sub>3</sub>, ITO<sub>(glass)</sub>/Cl-FAPbI<sub>3</sub>, and TiO<sub>2</sub>/Cl-FAPbI<sub>3</sub> heterojunction, respectively. The large hysteresis window in devices containing ITO/Cl-FAPbI<sub>3</sub> ([Supporting Information](#) Figure S6a,b) with different scanning rate and different scanning direction indicates an unbalance between electrons and holes transport in the device.<sup>6</sup> Contrarily, a negligible hysteresis and oscillation is observed in *J*–*V* curve of device with the TiO<sub>2</sub>/Cl-FAPbI<sub>3</sub> heterojunction ([Supporting Information](#) Figure S6c). Thus, it is reasonable to ascribe the oscillation to incongruous transport between photogenerated electrons and holes in the device. To further clarify the impact of chlorine on intrinsic characteristic of photoactive layer, [Supporting Information](#) Figure S7a,b shows the top-view SEM of FAPbI<sub>3</sub> and Cl-FAPbI<sub>3</sub> films with the same fabrication process as devices, respectively. However, no great difference in morphology is observed. It is worth to note that FAPbI<sub>3</sub> film showed a worse stability in air. And XRD profile showed obvious FAI residue in film as shown in [Supporting Information](#) Figure S7c indicating MACl had significant effect on FAPbI<sub>3</sub> formation as that to MAPbI<sub>3</sub><sup>40</sup> and the hydrophilic residue FAI made contribution to hydration.

In typical perovskite solar cells, charge carrier lifetimes within the charge selective layers play a vital role in the corresponding device performance because the carrier lifetime in the photoactive layer (perovskite) is large enough to reach the selective interface.<sup>43</sup> These selective materials in the device also act as the counter charge blocking layer to yield high charge collection efficiency. Thus, the collected charge lifetime in the ETL free devices should be short as the photogenerated holes in perovskite can come in direct contact with the electrons in the ITO layer (device A and B) because ITO is the conductor for both electron and hole. Here, we carried out transient photovoltage decay measurements to estimate the interfacial charge recombination process in devices. The obtained photovoltage decay of device B and C as a function of time is shown in [Figure 3b](#). As expected, a smaller time constant being 13 μs is gathered from the exponential fitting for device B. This result indicates the interfacial recombination in device B

**Table 1. Detailed Photovoltaic Parameters of the Flexible Cl-FAPbI<sub>3</sub> Device A (ITO<sub>(PET)</sub>/Cl-FAPbI<sub>3</sub> (350 nm)/Spiro-OMeTAD (150 nm)/Au (100 nm)) AM 1.5G Illumination (100 mW cm<sup>−2</sup> Light Intensity)**

		<i>V</i> <sub>OC</sub> /V	<i>J</i> <sub>SC</sub> /mAcm <sup>−2</sup>	FF	PCE/%
device A	fresh	0.955	20.70	0.64	12.70
device A	after 20 times bending	0.950	20.52	0.60	11.55



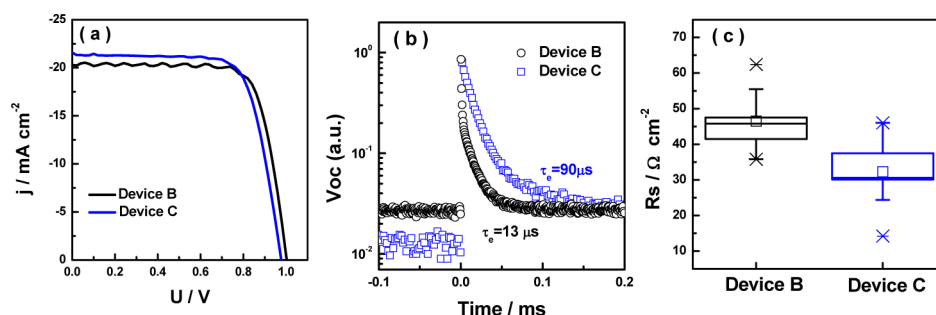


**Figure 3.** Photovoltaic performance and photogenerated carrier transport in devices B and C. (a)  $J$ – $V$  characteristics of devices using a metal mask with an aperture area of  $0.108 \text{ cm}^2$ , while the scan rate was kept at  $20 \text{ mV}$  per step with a delay time of  $0.001 \text{ s}$ . (b) Photovoltage decay plot for device B and C as a function of time with  $100 \text{ mW}$  LED bias, and (c) plot of average series resistance ( $R_s$ ) obtained from the  $J$ – $V$  plot of devices under AM 1.5G illumination according to Site's method. The devices were fabricated in planar structure, containing  $\text{ITO}_{(\text{glass})}/\text{Cl-FAPbI}_3(350 \text{ nm})/\text{spiro-OMeTAD}(150 \text{ nm})/\text{Au}(100 \text{ nm})$  in device B and  $\text{ITO}_{(\text{glass})}/\text{TiO}_2(40 \text{ nm})/\text{Cl-FAPbI}_3(350 \text{ nm})/\text{spiro-OMeTAD}(150 \text{ nm})/\text{Au}(100 \text{ nm})$  in device C.

**Table 2. Detailed Photovoltaic Parameters of Devices under AM 1.5G Illumination ( $100 \text{ mW cm}^{-2}$  Light Intensity)<sup>a</sup>**

	$V_{OC}/V$	$J_{sc}/\text{mAcm}^{-2}$	FF	PCE/%
device B	1.00	20.29	0.76	15.49
device C	0.98	21.57	0.75	15.32

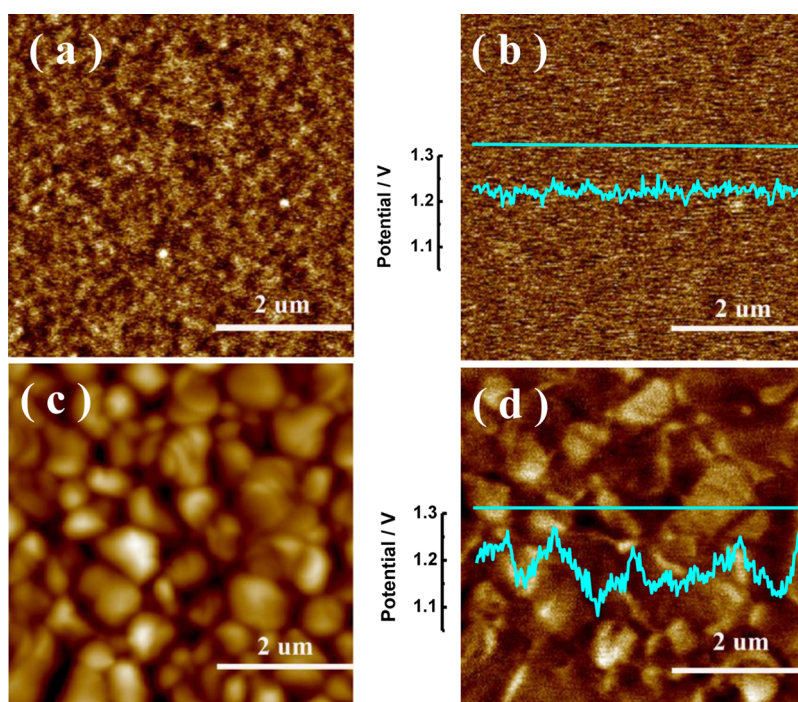
<sup>a</sup>Planar device contains  $\text{ITO}_{(\text{glass})}/\text{Cl-FAPbI}_3(350 \text{ nm})/\text{Spiro-OMeTAD}(150 \text{ nm})/\text{Au}(100 \text{ nm})$  labeled device B,  $\text{ITO}_{(\text{glass})}/\text{TiO}_2(40 \text{ nm})/\text{Cl-FAPbI}_3(350 \text{ nm})/\text{Spiro-OMeTAD}(150 \text{ nm})/\text{Au}(100 \text{ nm})$  coded as device C.

is worse compared to that in device C with  $\text{TiO}_2$  acting as hole-blocking layer, whose time constant in interfacial recombination is  $90 \mu\text{s}$ .

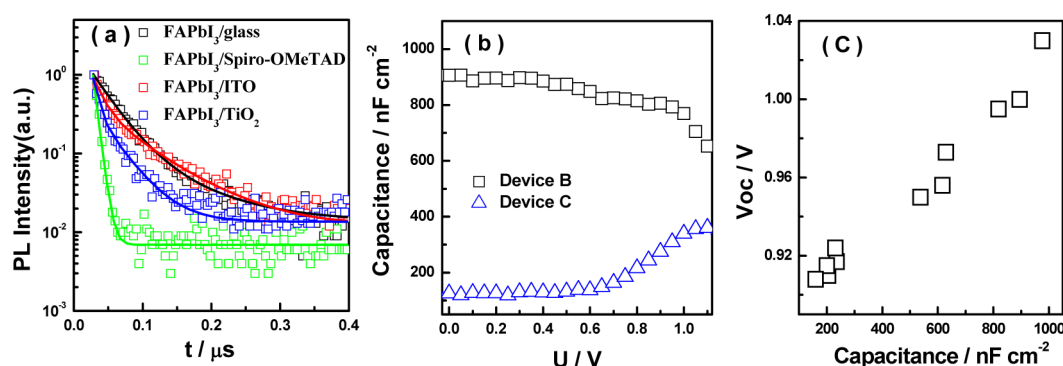
A general single diode model was used, according to Site's method,<sup>44</sup> to evaluate the photogenerated charge transporting properties of flexible devices under AM1.5G illumination.

Figure 3c shows the statistics of fitting results of series resistance ( $R_s$ ). The average  $R_s$  in device B is about  $45 \Omega/\text{cm}^2$ , larger than that ( $\sim 32 \Omega/\text{cm}^2$ ) in device C with  $\text{TiO}_2$  compact layer on rigid ITO/glass. This result goes against our expectation because ITO is more conductive than semiconductor  $\text{TiO}_2$  layer. To clarify the reason for enlarging the  $R_s$ , the  $R_s$  statistics in devices in dark with different spin-coating rate for FAI is presented in Supporting Information Figure S8. The results indicate that the large  $R_s$  is not caused by excess FAI or ITO corroded by FAI. Here, the results obtained from photovoltage decay and  $R_s$  indicates perovskite/ITO heterojunction has negative influence on carriers (electrons) transport. However, it is interesting to see the device based on such a heterojunction still give rise to photovoltaic performance.

In perovskite solar cells, there are two common mechanisms for photogenerated charge transport: one is the accumulation-diffusion model following dye-sensitized solar cells (DSCs)<sup>45</sup> in



**Figure 4.** Kelvin probe force microscopy (KPFM) measurement. (a,c) Two-dimensional topography spatial maps, and (b,d) two-dimensional surface potential spatial maps for ITO substrate and  $\text{Cl-FAPbI}_3$ , respectively. Insets show variations in local CPD across the sample surface.



**Figure 5.** Photogenerated carrier extraction and capacitance in device. (a) Photoluminescence decay curves of Cl-FAPbI<sub>3</sub> perovskite films on different quenching layers. (b) Capacitance–voltage plot for devices B and C. (c) statistics of relationship between  $V_{OC}$  and capacitance in different devices, where the capacitance is obtained at 0 V.

which perovskite acts as a sensitizer and charges are transferred by carrier-selective materials; another is due to a charge shifting in perovskite with the assistance of built-in potential as in p–i–n type solar cells.<sup>46</sup> For the former, the driving force originates from a carrier concentration gradient, while the electric field originating from space charge in the depleted layer is the main force for the latter. Thus, understanding the role of the heterojunctions in the device is critical for further understanding device working principles. First, we conducted the ultraviolet photoelectron spectrum (UPS) measurement for our as-synthesized Cl-FAPbI<sub>3</sub> to clearly observe the electric structure. Supporting Information Figure S9 depicts the UPS of the surface measurement for Cl-FAPbI<sub>3</sub>/ITO substrate. Insert is cutoff energy ( $E_{cutoff}$ ) regions. The  $E_{cutoff}$  is 16.6 eV, and the work function is estimated to be 4.6 eV by using the equation  $E_{WF} = 21.2 - E_{cutoff}$ . Herein, it is worth remarking that Cl-FAPbI<sub>3</sub> can be treated as an n-type semiconductor and a p–n junction may form at the Cl-FAPbI<sub>3</sub>/spiro-OMeTAD heterojunction.

KPFM was then employed to investigate the Cl-FAPbI<sub>3</sub>/ITO heterojunction. Figure 4 shows the topography and potential spatial maps of ITO and Cl-FAPbI<sub>3</sub>. A small roughness of 1.4 nm in the ITO film can be obtained from height image in Figure 4a. According to Figure 4c, the roughness of Cl-FAPbI<sub>3</sub> film is 19.1 nm, indicating a comparable uniform and compact layer loaded on ITO. The smoothness of the layer could be an important factor that enables efficient photogenerated charge dissociation/transport in perovskite solar cells. As shown in Figure 5b,d, the two-dimensional image overlaying the surface potential spatial on the topographical image of Cl-FAPbI<sub>3</sub> shows an apparent difference between the grain boundaries and the bulk. Moreover, the relative values in surface work function of ITO and Cl-FAPbI<sub>3</sub> can also be determined by the contact potential difference (CPD)<sup>47</sup>

$$V_{CPD} = \frac{(\phi_{tip} - \phi_{sample})}{e}$$

Where  $\phi_{sample}$  and  $\phi_{tip}$  are the work functions of the sample and tips, and  $e$  is the element charge. Using the same scanning tip during the measurement,  $\phi_{tip}$  can be treated as a constant value. Referring to inserted potential line in Figure 5b,d, the CPD of both ITO and Cl-FAPbI<sub>3</sub> are  $\sim 1.2$  V. The difference of energy level in two materials is insufficient to form a built-in potential.<sup>48</sup>

Photoluminescence (PL) decay transient spectra of Cl-FAPbI<sub>3</sub> films with a peak emission wavelength of 805 nm was

conducted to determine carrier lifetimes and quenching effects via transport layers. The transient PL spectra of Cl-FAPbI<sub>3</sub> films with different quenching layers are presented in Figure 5a from which time constant ( $\tau$ ) was obtained from exponential fitting. The PL decay of the neat Cl-FAPbI<sub>3</sub> film on glass exhibits  $\tau$  of  $68 \pm 2$  ns, which is comparable to that of previous studies.<sup>43,49</sup> Transient PL decay of Cl-FAPbI<sub>3</sub> on ITO nearly overlaps that of Cl-FAPbI<sub>3</sub> on glass with only a small difference at the beginning, indicating a poor quenching effect of ITO to Cl-FAPbI<sub>3</sub>. It is worth noting that the result is contrary to that of FTO, since FTO is an effective quencher (seeing Supporting Information Figure S10). As shown in Figure 5a, the addition of TiO<sub>2</sub> and Spiro-OMeTAD as electron and hole quenching layers on Cl-FAPbI<sub>3</sub> film can accelerate the PL decay, with observed  $\tau$  of  $14 \pm 2$  ns and  $6 \pm 1$  ns, respectively. It has also been shown that free carriers can be generated in the Cl-FAPbI<sub>3</sub> films at room temperature and subsequently transfer to the selective materials without assistance from a heterojunction.<sup>50</sup> As a result, the PL decay in the Cl-FAPbI<sub>3</sub> film originates from the free carrier extraction or recombination. Thus, ITO is not an effective quencher in device A and B, where the holes are extracted significantly more efficiently by spiro-OMeTAD. Considering the similar contact area between Cl-FAPbI<sub>3</sub>/ITO and Cl-FAPbI<sub>3</sub>/spiro-OMeTAD in full devices (both device A and B), the photogenerated positive carriers (holes) under illumination should be rapidly extracted to the external circuit, resulting in a large amount of electrons left behind due to slow extraction by ITO. This result also coincides with the interpretation to the oscillation and hysteresis in  $J$ – $V$  curve indicating ITO/Cl-FAPbI<sub>3</sub> heterojunction has a significant influence on device operation.

In order to further understand the device operation mechanism, we conducted capacitance–voltage ( $C$ – $V$ ) measurements on devices at 1000 Hz in the dark. Figure 5b compares the capacitance for device B and C under various bias conditions. Under the same bias, the capacitance in device B is almost 1 order of magnitude larger than that in device C. A large capacitance indicates a large charge storage. Referring to the difference in device B and C, the large charge storage is caused by the Cl-FAPbI<sub>3</sub>/ITO heterojunction and charge carriers should presumably be stored in Cl-FAPbI<sub>3</sub> close to the Cl-FAPbI<sub>3</sub>/ITO heterojunction, because ITO is a metallic material with a high conductivity. The large electron storage due to the large capacitance increases the electron quasi-Fermi level in the Cl-FAPbI<sub>3</sub>, which produces an energy level difference from the hole quasi-Fermi level in spiro-OMeTAD

to form a photovoltage. A similar phenomenon is observed in the device containing ITO/Cl-FAPbI<sub>3</sub>/spiro-OMeTAD (as seen in Supporting Information Figure S11) indicating a same work mechanism. Figure 5c gives a statistical relationship between capacitance in dark and  $V_{OC}$  of the device B, showing that  $V_{OC}$  increases with the capacitance. Furthermore, concentration gradient due to electron storage in Cl-FAPbI<sub>3</sub> is proposed to form an electric field along Cl-FAPbI<sub>3</sub>/ITO heterojunction that provides the driving force for the charge transferring from Cl-FAPbI<sub>3</sub> to ITO. In order to confirm the hypothesis, we fabricated a device based on a different architecture of ITO<sub>(glass)</sub>/Cl-FAPbI<sub>3</sub>/PCBM/Au. PCBM is phenyl-C61-butyric acid methyl ester, an n-type material that can rapidly extract electrons from perovskite.<sup>19</sup> Supporting Information Figure S12 shows the  $I$ - $V$  plot of this device, which achieved a PCE of 3.1% while  $V_{OC}$  of 0.766 V was observed. This result contradicts traditional p-i-n devices because PCBM has large electron affinity and good electron transport property, opposite to spiro-OMeTAD. Similarly to the situation in device A and B, after the electron is extracted by PCBM a large amount of holes remain in Cl-FAPbI<sub>3</sub> that allows the concentration gradient to drive holes from Cl-FAPbI<sub>3</sub> to the ITO substrate. As a result, we can see that charge storage is important for device operation without an electron or hole selective layer.

As mentioned above, PbI<sub>2</sub> formed within the Cl-FAPbI<sub>3</sub> film via releasing the organic species is assumed to be responsible for device operation. Here, the role of PbI<sub>2</sub> in device performance was estimated by the relation between device PCE statistics and the amount of PbI<sub>2</sub>. As shown in Supporting Information Figure S13, the PbI<sub>2</sub> amount would increase as Cl-FAPbI<sub>3</sub> annealing time increases, while the device performance reaches the optimal condition with Cl-FAPbI<sub>3</sub> annealed for 40 min. As shown in Supporting Information Figure S14, with an optimizing annealing procedure with higher temperature of 135 °C a comparable performance can be obtained with shorter annealing time. With prolonging the annealing time, an obvious degradation of Cl-FAPbI<sub>3</sub> into PbI<sub>2</sub> is also observed. Because of valence/conduction band of Cl-FAPbI<sub>3</sub> localizing in bandgap of PbI<sub>2</sub>, PbI<sub>2</sub> formed at the surface can accelerate the charge stored in Cl-FAPbI<sub>3</sub> and inhabit the opposite charge in perovskite recombining with the charge on ITO.<sup>51,52</sup>

In conclusion, we report a simple device architecture for flexible perovskite solar cells without ETL. An efficient performance with PCE of 12.70% was achieved. This flexible device shows great potential for large-scale production of solar cells via roll-to-roll manufacturing. With accurate measurement, it is assumed that the built-in potential across the perovskite/ITO heterojunction is not essential for the perovskite device operation, while a large charge storage in the perovskite film is believed to ensure the photovoltage and provides the driving force for charge transfer across this interface. Meanwhile, the other heterojunction, for example, Cl-FAPbI<sub>3</sub>/spiro-OMeTAD heterojunction in device A and B, is important for device operation as it can be replaced by other effective quenching layers. This result indicates the possibility for further simplification of device structures and that materials with high conductivity can be applied in perovskite-based photovoltaic devices. Our work provides guidance for the development of large-scale roll-to-roll manufacturing of high performance perovskite solar cells.

**Materials and Methods. Synthesis of FAI.** FAI was prepared by mixing 3 g of formamidine acetate and 8.2 g HI

aqueous solution (45 wt % in water) at 0 °C for 2 h. The precipitate was collected by rotary thermal evaporation. The collected precipitate was dissolved in the hot mixture solvent of ethanol and diethyl ether to form a saturated solution and then the solution was kept in a refrigerator at -3 °C. The white precipitate was collected by filtration and was dried at 60 °C under vacuum for 2 days. XRD profile of fresh FAI is presented in Supporting Information Figure S15.

**Device Fabrication.** The ITO<sub>(PET)</sub> (South China Xiang Science & Technology Company Limited,  $R \sim 8\Omega/\square$ ,  $T \sim 78\%$ ) was treated with UV-ozone for 30 min then immediately transferred to a dry-air glovebox. The PbI<sub>2</sub> solution (0.46g mL<sup>-1</sup>) was spin-coated at 3000 rpm for 30 s and then annealed at 343.15 K for 20 min. After cooled to room temperature, the solution mixing FAI and MACl (50:5; FAI:MACl) was coated at 3000 rpm for 30 s. Then the film was transferred out of the glovebox and heated at 393.15 K in air for 40 min. Afterward, the film was transferred back to the glovebox immediately, where the spiro-OMeTAD was spin-coated with 3000 rpm for 30 s on the film. Finally, the gold was evaporated as a counter electrode. The results of optimizing this process for devices with ITO<sub>(glass)</sub> (Courtaulds Performance Films,  $R \sim 20\Omega/\square$ ,  $T \sim 92\%$ ) can be found in Supporting Information Figures S16–S18.

**Photovoltaic Characterization.** A 1000 W xenon light source solar simulator (Oriel, model 9119) with AM 1.5G filter (Oriel, model 91192) was used to provide an irradiance of 100 mW cm<sup>-2</sup> at the surface of the solar cell. The current–voltage characteristics of the cell under these conditions were obtained by applying external potential bias to the cell and measuring the generated photocurrent with a Keithley model 2400 digital source meter. All devices were scanned by reverse direction with 20 mV per step with a delay time of 0.001 s unless noted otherwise.

**C–V analysis.** The C–V plot was obtained from a Hewlett-Packard 4284A LCR meter. Electrical contact to the devices during LCR measurements was provided by a Janis cryogenic probe station.

## ■ ASSOCIATED CONTENT

### ● Supporting Information

The Supporting Information is available free of charge on the ACS Publications website at DOI: 10.1021/acs.nanolett.5b02126.

Additional data and figures. (PDF)

## ■ AUTHOR INFORMATION

### Corresponding Authors

\*E-mail: (Y.Y.) yangy@ucla.edu..

\*E-mail: (M.W.) mingkui.wang@mail.hust.edu.cn

### Author Contributions

The manuscript was written through contributions of all authors. All authors have given approval to the final version of the manuscript.

X.X. and Q.C. contributed equally to this work.

### Notes

The authors declare no competing financial interest.

## ■ ACKNOWLEDGMENTS

Financial support from Air Force Office of Scientific Research (AFOSR, Grant FA9550-09-1-0610), and National Science Foundation (NSF ECCS-1202231), and the director Fund of



China Scholarship Council (no. 201406160004), the WNLO, the 973 Program of China (2014CB643506, 2013CB922104, and 2011CBA00703), the NSFC (21161160445, and 21173091) are acknowledged.

## REFERENCES

- (1) Weber, D.  $\text{CH}_3\text{NH}_3\text{PbX}_3$ , ein Pb(II)-system mit kubischer perowskitstruktur. *Z. Naturforsch.* **1978**, *33*, 1443–1445.
- (2) Kim, H.; Lee, C.; Im, J.; Lee, K.; Moehl, T.; Marchioro, A.; Moon, S.; Humphry-Baker, R.; Yum, J.; Moser, J.; Grätzel, M.; Park, N. *Sci. Rep.* **2012**, *2* (591), 1–7.
- (3) Hu, X.; Zhang, X.; Liang, L.; Bao, J.; Li, S.; Yang, W.; Xie, Y. *Adv. Funct. Mater.* **2014**, *24*, 7373–7380.
- (4) Gil-Escrig, L.; Longo, G.; Pertegás, A.; Roldán-Carmona, C.; Soriano, A.; Sessolo, M.; Bolink, H. *Chem. Commun.* **2015**, *51*, 569–571.
- (5) Chondroudis, K.; Mitzi, D. *Chem. Mater.* **1999**, *11*, 3028–3030.
- (6) Jeon, N.; Noh, J.; Yang, W.; Kim, Y.; Ryu, S.; Seo, J.; Seok, S. *Nature* **2015**, *517*, 476–480.
- (7) Xu, X.; Liu, Z.; Zuo, Z.; Zhang, M.; Zhao, Z.; Shen, Y.; Zhou, H.; Chen, Q.; Yang, Y.; Wang, M. *Nano Lett.* **2015**, *15*, 2402–2408.
- (8) Yang, W.; Noh, J.; Jeon, N.; Kim, Y.; Ryu, S.; Seo, J.; Seok, S. *Science* **2015**, *348*, 1234–1237.
- (9) Kojima, A.; Teshima, K.; Shirai, Y.; Miyasaka, T. *J. Am. Chem. Soc.* **2009**, *131*, 6050–6051.
- (10) Lee, M.; Teuscher, J.; Miyasaka, T.; Murakami, T.; Snaith, H. *Science* **2012**, *338*, 643–647.
- (11) Liu, D.; Kelly, T. *Nat. Photonics* **2014**, *8*, 133–138.
- (12) Burschka, J.; Pellet, N.; Moon, S.; Humphry-Baker, R.; Gao, P.; Nazeeruddin, M.; Grätzel, M. *Nature* **2013**, *499*, 316–319.
- (13) Zhou, H.; Chen, Q.; Li, G.; Luo, S.; Song, T.; Duan, H.; Hong, Z.; You, J.; Liu, Y.; Yang, Y. *Science* **2014**, *345*, 542–546.
- (14) Xu, X.; Zhang, H.; Cao, K.; Cui, J.; Lu, J.; Zeng, X.; Shen, Y.; Wang, M. *ChemSusChem* **2014**, *7*, 3088–3094.
- (15) Liu, M.; Johnston, M.; Snaith, H. *Nature* **2013**, *501*, 395–398.
- (16) Wojciechowski, K.; Saliba, M.; Leijtens, T.; Abate, A.; Snaith, H. *Energy Environ. Sci.* **2014**, *7*, 1142–1147.
- (17) Roldán-Carmona, C.; Malinkiewicz, O.; Soriano, A.; Espallargas, G.; Garcia, A.; Reinecke, P.; Kroyer, T.; Dar, M.; Nazeeruddin, M.; Bolink, H. *Energy Environ. Sci.* **2014**, *7*, 994–997.
- (18) Docampo, P.; Ball, J.; Darwich, M.; Eperon, G.; Snaith, H. *Nat. Commun.* **2013**, *4* (2761), 1–6.
- (19) You, J.; Hong, Z.; Yang, Y.; Chen, Q.; Cai, M.; Song, T.; Chen, C.; Lu, S.; Liu, Y.; Zhou, H.; Yang, Y. *ACS Nano* **2014**, *8*, 1674–1680.
- (20) Hwang, K.; Jung, Y.; Heo, Y.; Scholes, F.; Watkins, S.; Subbiah, J.; Jones, D.; Kim, D.; Vak, D. *Adv. Mater.* **2015**, *27*, 1241–1247.
- (21) Kumar, M.; Yantara, N.; Dharani, S.; Grätzel, M.; Mhaisalkar, S.; Boix, P.; Mathews, N. *Chem. Commun.* **2013**, *49*, 11089–11091.
- (22) Etgar, L.; Gao, P.; Xue, Z.; Peng, Q.; Chandiran, A.; Liu, B.; Nazeeruddin, M.; Grätzel, M. *J. Am. Chem. Soc.* **2012**, *134*, 17396–17399.
- (23) Ku, Z.; Rong, Y.; Xu, M.; Liu, T.; Han, H. *Sci. Rep.* **2013**, *3* (3132), 1–5.
- (24) Ke, W.; Fang, G.; Wan, J.; Tao, H.; Liu, Q.; Xiong, L.; Qin, P.; Wang, J.; Lei, H.; Yang, G.; Qin, M.; Zhao, X.; Yan, Y. *Nat. Commun.* **2015**, *6* (6700), 1–7.
- (25) Liu, D.; Yang, J.; Kelly, T. *J. Am. Chem. Soc.* **2014**, *136*, 17116–17122.
- (26) Kim, H.; Mora-Sero, I.; Gonzalez-Pedro, V.; Fabregat-Santiago, F.; Juarez-Perez, E.; Park, N.; Bisquert, J. *Nat. Commun.* **2013**, *4* (2242), 1–7.
- (27) Aharon, S.; Gamliel, S.; Cohen, B.; Etgar, L. *Phys. Chem. Chem. Phys.* **2014**, *16*, 10512–10518.
- (28) Liu, Z.; Zhang, M.; Xu, X.; Bu, L.; Zhang, W.; Li, W.; Zhao, Z.; Wang, M.; Cheng, Y.; He, H. *Dalton Trans.* **2015**, *44*, 3967–3973.
- (29) Pang, S.; Hu, H.; Zhang, J.; Lv, S.; Yu, Y.; Wei, F.; Qin, T.; Xu, H.; Liu, Z.; Cui, G. *Chem. Mater.* **2014**, *26*, 1485–1491.
- (30) Kawabata, Y.; Yoshizawa-Fujita, M.; Takeoka, Y.; Rikukawa, M. *Synth. Met.* **2009**, *159*, 776–779.
- (31) Eperon, G.; Stranks, S.; Menelaou, C.; Johnston, M.; Herz, L.; Snaith, H. *Energy Environ. Sci.* **2014**, *7*, 982–988.
- (32) Pellet, N.; Gao, P.; Gregori, G.; Yang, T.; Nazeeruddin, M.; Maier, J.; Grätzel, M. *Angew. Chem., Int. Ed.* **2014**, *53*, 3151–3157.
- (33) Park, N. *J. Phys. Chem. Lett.* **2013**, *4*, 2423–2429.
- (34) Lee, J.; Seol, D.; Cho, A.; Park, N. *Adv. Mater.* **2014**, *26*, 4991–4998.
- (35) Colella, S.; Mosconi, E.; Pellegrino, G.; Alberti, A.; Guerra, V.; Masi, S.; Listorti, A.; Rizzo, A.; Condorelli, G.; de Angelis, F.; Gigli, G. *J. Phys. Chem. Lett.* **2014**, *5*, 3532–3538.
- (36) Stranks, S.; Eperon, G. E.; Grancini, G.; Menelaou, C.; Alcocer, M.; Leijtens, T.; Herz, L.; Petrozza, A.; Snaith, H. *Science* **2013**, *342*, 341–344.
- (37) Kim, S.; Lee, J. *J. Appl. Phys.* **2004**, *95*, 2560–2563.
- (38) Lv, S.; Pang, S.; Zhou, Y.; Padture, N.; Hu, H.; Wang, L.; Zhou, X.; Zhu, H.; Zhang, L.; Huang, C.; Cui, G. *Phys. Chem. Chem. Phys.* **2014**, *16*, 19206–19211.
- (39) Yang, J.; Siempelkamp, B.; Liu, D.; Kelly, T. *ACS Nano* **2015**, *9*, 1955–1963.
- (40) Chen, Q.; Zhou, H.; Fang, Y.; Stieg, A.; Song, T.; Wang, H.; Xu, X.; Liu, Y.; Lu, S.; You, J.; Sun, P.; McKay, J.; Goorsk, M.; Yang, Y. *Nat. Commun.* **2015**, *6* (7269), 1–9.
- (41) Xu, X.; Li, S.; Zhang, H.; Shen, Y.; Zakeeruddin, S.; Graetzel, M.; Cheng, Y.; Wang, M. *ACS Nano* **2015**, *9*, 1782–1787.
- (42) Yang, X.; Yanagida, M.; Han, L. *Energy Environ. Sci.* **2013**, *6*, 54–66.
- (43) Xing, G.; Mathews, N.; Sun, S.; Lim, S.; Lam, Y.; Grätzel, M.; Mhaisalkar, S.; Sum, T. *Science* **2013**, *342*, 344–347.
- (44) Hegedus, S.; Shafarman, W. *Prog. Photovoltaics* **2004**, *12*, 155–176.
- (45) Gonzalez, V.; Juarez-Perez, E.; Arsyad, W.; Barea, E.; Fabregat-Santiago, F.; Mora-Sero, I.; Bisquert, J. *Nano Lett.* **2014**, *14*, 888–893.
- (46) Pattantyus-Abraham, A.; Kramer, I.; Barkhouse, A.; Wang, X.; Konstantatos, G.; Debnath, R.; Levina, L.; Raabe, I.; Nazeeruddin, M.; Grätzel, M.; Sargent, E. *ACS Nano* **2010**, *4*, 3374–3380.
- (47) Melitz, W.; Shen, J.; Kummel, A.; Lee, S. *Surf. Sci. Rep.* **2011**, *66*, 1–27.
- (48) Laban, W.; Etgar, L. *Energy Environ. Sci.* **2013**, *6*, 3249–3253.
- (49) Stranks, S.; Eperon, G.; Grancini, G.; Menelaou, C.; Alcocer, M.; Leijtens, T.; Herz, L.; Petrozza, A.; Snaith, H. *Science* **2013**, *342*, 341–344.
- (50) Lo, M.; Guan, Z.; Ng, T.; Chan, C.; Lee, C. *Adv. Funct. Mater.* **2015**, *25*, 1213–1218.
- (51) Chen, Q.; Zhou, H.; Song, T.; Luo, S.; Hong, Z.; Duan, H.; Dou, L.; Liu, Y.; Yang, Y. *Nano Lett.* **2014**, *14*, 4158–4163.
- (52) Cao, D.; Stoumpos, C.; Malliakas, C.; Katz, M.; Farha, O.; Hupp, J.; Kanatzidis, M. *APL Mater.* **2014**, *2*, 091101.